

# Unveiling the Complex Magnetization Reversal Process in 3D Nickel Nanowire Networks

Alejandra Ruiz-Clavijo, Olga Caballero-Calero, David Navas, Amanda A. Ordoñez-Cencerrado, Javier Blanco-Portals, Francesca Peiró, Ruy Sanz,\* and Marisol Martín-González\*

Understanding the interactions among magnetic nanostructures is one of the key factors to predict and control the advanced functionalities of 3D integrated magnetic nanostructures. In this work, the focus is on different interconnected Ni nanowires forming an intricate, but controlled, and ordered magnetic system: Ni 3D Nanowire Networks (3DNNs). These self-ordered systems present striking anisotropic magnetic responses, depending on the interconnections' position between nanowires. To understand their collective magnetic behavior, the magnetization reversal processes are studied within different Ni 3D Nanowire Networks compared to the 1D nanowire 1DNW array counterparts. The systems are characterized at different angles using first magnetization curves, hysteresis loops, and First Order Reversal Curves techniques, which provided information about the key features that enable macroscopic tuning of the magnetic properties of the 3D nanostructures. In addition, micromagnetic simulations endorse the experiments, providing accurate modeling of their magnetic behavior. The results reveal a plethora of magnetic interactions, neither evident nor intuitive, which are the main role players controlling the collective response of the system. The results pave the way for the design and realization of 3D novel metamaterials and devices based on the nucleation and propagation of ferromagnetic domain walls both in 3D self-ordered systems and future nano-lithographed devices.

we are being forced to look forward to the development of new materials or geometries that satisfy these requirements. For years, technology has been mainly based on the use of planar devices, but the improvement of the third dimension, or 3D systems, is the natural step in the next technological revolution. In particular, 3D magnetic nanostructures have received significant attention due to the possibility to exhibit and control new and fascinating properties.<sup>[1]</sup> Their rapid development is based on the improvement of both the fabrication and characterization techniques. For example, 3D direct writing, by using focused electron or ion beam-induced deposition techniques (FEBID and FIBID),<sup>[2]</sup> is one of the most outstanding methodologies for the fabrication of complex-shaped 3D magnetic nanoelements with resolutions down to a few tens of nm.<sup>[3]</sup> Alternative techniques, that have shown great potential, are based on 3D templates such as those prepared by two-photon direct-write optical lithography<sup>[4]</sup> or self-assembled methodologies.<sup>[5]</sup>

In this work, we study the magnetic behavior of 3D Ni interconnected nanowire arrays prepared by electrodeposition in self-assembled 3D alumina templates (3D-AAO).<sup>[5c,6]</sup> The electrodeposition of ferromagnetic nanowires (NWs) in polycarbonate membranes was first reported

## 1. Introduction

The current social needs require the development of smaller, faster, and more energy-efficient devices. In this framework,

A. Ruiz-Clavijo, O. Caballero-Calero, M. Martín-González  
Instituto de Micro y Nanotecnología  
IMN-CNM  
CSIC (CEI UAM+CSIC) Isaac Newton  
Tres Cantos, Madrid 8, E-28760, Spain  
E-mail: marisol.martin@csic.es

D. Navas  
Instituto de Ciencia de Materiales de Madrid  
ICMM-CSIC  
Madrid 28049, Spain

A. A. Ordoñez-Cencerrado, R. Sanz  
National Institute for Aerospace Technology (INTA)  
Payloads and Space Science Department  
Space Magnetism Area, Torrejón de Ardoz, Madrid 28850, Spain  
E-mail: sanzgr@inta.es

J. Blanco-Portals, F. Peiró  
LENS-MIND  
Department of Electronics and Biomedical Engineering  
Universitat de Barcelona  
Barcelona 08028, Spain

J. Blanco-Portals, F. Peiró  
Institute of Nanoscience and Nanotechnology (IN2UB)  
Universitat de Barcelona  
Barcelona 08028, Spain

 The ORCID identification number(s) for the author(s) of this article can be found under <https://doi.org/10.1002/aelm.202200342>.

© 2022 The Authors. Advanced Electronic Materials published by Wiley-VCH GmbH. This is an open access article under the terms of the Creative Commons Attribution-NonCommercial-NoDerivs License, which permits use and distribution in any medium, provided the original work is properly cited, the use is non-commercial and no modifications or adaptations are made.

DOI: 10.1002/aelm.202200342

in 1993 by Whitney et al.<sup>[7]</sup> Since then, parallel nanowire arrays have been prepared in different kinds of templates, such as in polycarbonate etched ion-track membranes<sup>[8]</sup> or nanoporous anodic alumina templates.<sup>[9]</sup> Both types of porous systems have been already used for the fabrication of 3D nanostructured templates.<sup>[5c,10]</sup> While polycarbonate etched ion-track membranes give rise to random 3D ferromagnetic networks of interconnected nanowires tilted at different angles (up to 45° to the surface normal),<sup>[11]</sup> standard hexagonally ordered parallel ferromagnetic nanowires are interconnected with perpendicular or transversal nanowires (TNWs) in 3D nanoporous anodic alumina templates.<sup>[12]</sup>

Self-assembled synthesis approaches outperform lithography techniques in achievable patterned macroscopic size and economic performance at the cost of sacrificing design options and resolution. Therefore, a trade-off should be performed depending on the targeted application. Nevertheless, self-ordered systems, due to their simplified and agile synthesis, offer suitable initial experimental systems for basic research. Regarding the technological applications, ferromagnetic networks were firstly suggested for the development of magnetic domain-wall racetrack memories.<sup>[13]</sup> In addition, other interesting applications are being currently explored such as microwave absorbing metamaterials,<sup>[11a]</sup> for which areas above cm<sup>2</sup> are demanded, magnetic sensor and logic devices,<sup>[11c]</sup> spin caloritronic devices,<sup>[11d,e]</sup> artificial spin-ice systems with magnetic frustration,<sup>[14]</sup> and even for artificial neural networks.<sup>[15]</sup> The fabrication of high-quality structures with well-controlled periodicities along the three directions in the nanoscale opens also the possibility to develop 3D magnonic crystals, where the vertical dimension will increase the density of elements as well as generate new functionalities for using spin waves to transmit, store, and process information.<sup>[16]</sup> In addition, it should be noted that our ferromagnetic networks are made up of cylindrical nanowires, which have been suggested as the key elements for the development and understanding of a new research field known as magnetism in curved geometry.<sup>[17]</sup> Literature shows that the curved geometry in cylindrical nanowires can lead to novel and non-trivial magnetic phenomena such as the formation of skyrmion magnetic configurations<sup>[18]</sup> or Bloch-point domain walls.<sup>[19]</sup>

Then, this work aims to provide an insight into the understanding of the observed complex magnetic behavior of Ni 3D Nano Networks (3DNNs) electrodeposited in 3D porous alumina templates. This methodology, compared to other techniques for the fabrication of 3D networks,<sup>[11]</sup> reduces the stochastic arrangement, allowing to control of the number and distance of the transversal nanowires over large areas (samples with up to a few cm<sup>2</sup>) by using a basic electrochemistry laboratory infrastructure. We have performed a consistent magnetic characterization of Ni nanowires (NWs) arrays and Ni 3DNNs with two different periods between transversal wires. The study combines the analysis of experimental hysteresis loops, First Order Reverse Curves (FORC), and micromagnetic simulations. The complexity of the magnetization reversal process and how it is modified by the presence and the period of TNWs is studied. The outcome provides a modeled framework of magnetization dynamics endorsed by experimental results. This framework is a satisfactory approach to explaining the observed magnetic response of self-ordered

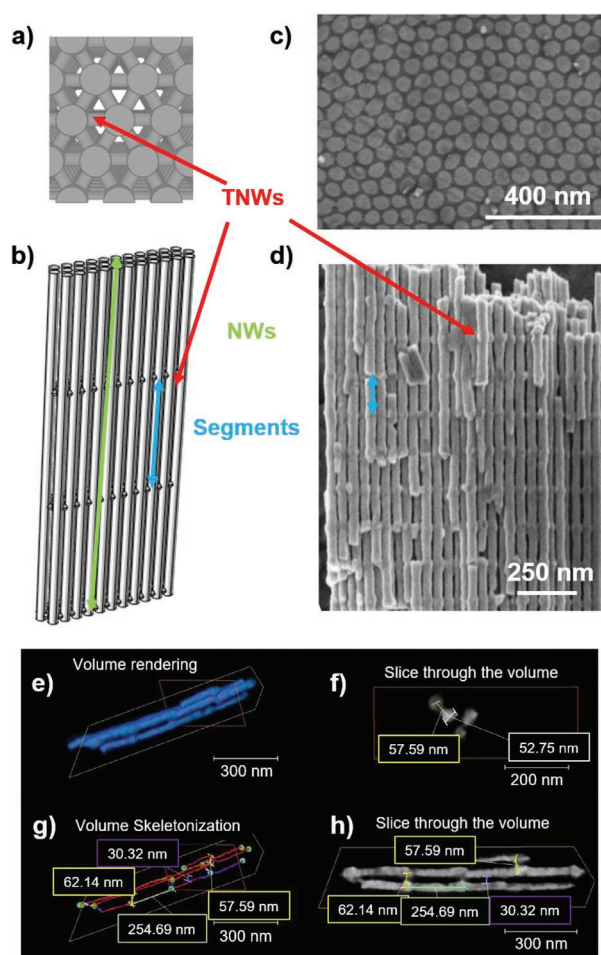


**Figure 1.** Schematic views of a 3DNN structure: a) top view (diagram of the elements used in the computational simulations) and b) cross-section. SEM images of c) the top view after mechanical polishing of the alumina matrix, d) the cross-section of 3DNN255 with 255 nm of the period between transversal nanowires, after the dissolution of the alumina matrix. TNWs are indicated by red arrows, NWs are in green, and segments are in blue. (e–h) show the TEM tomography reconstruction of sample 3DNN255 after alumina dissolution and sonication, being (e) the volume rendering with the planes of the slices shown in the other figures. g) Skeletonization of the volume, which represents the continuous connections in the reconstructed volume. f) Perpendicular and h) longitudinal slices through the volume. Some measurements are marked in them for the distances between TNCs, which oscillated around 255 nm.

systems and a powerful tool for designing and predicting future magnetic devices based on 3D interconnected nanowires obtained by high-resolution techniques.

## 2. Results and Discussion

Nickel 3DNNs morphology is described in the diagrams shown in **Figure 1a,b**, and it is confirmed by Scanning Electron Microscope (SEM) micrographs (**Figure 1c,d**). It is demonstrated that Ni has successfully filled the 3D alumina porous structure and generated 3D interconnected nanomeshes. The standard hexagonal closed packed (hcp) ordering is observed in our Ni

**Table 1.** Geometric characterization of the samples:  $P$  is the periodicity between TNWs,  $L$  is the total NWs' length,  $D$  is the inter-wire distance,  $d$  is the NWs diameter,  $dT$  is the TNWs diameter and  $N$  is the number of TNWs levels.

Sample	$P$ [nm]	$L$ [ $\mu$ m]	$D$ [nm]	$d$ [nm]	$dT$ [nm]	$N$
Nanowire array	–	24	65	$55 \pm 5$	–	0
3DNN445	$445 \pm 10$	25	64	53	$28 \pm 3$	56
3DNN255	$255 \pm 10$	5.3	62	54	30	20

NW arrays (see Figure 1c). Cylindrical NWs grow parallel to each other and perpendicular to the alumina template surface (Figure 1b,d). An average diameter of  $(55 \pm 5)$  nm and an inter-wire distance of 65 nm were estimated from the SEM images of the Ni NWs with several  $\mu$ m lengths. Moreover, the electron tomography experiments confirmed the columnar structure with sizes well in accordance with the SEM findings (see Figure 1e–h) corroborating the above-mentioned dimensions.

SEM imaging confirms also that transversal nanowires (TNWs) are distributed along the nanowires in levels separated by a periodicity ( $P$ ) of 255 nm (Figure 1d) or 445 nm. TNWs surround each Ni nanowire by a hexagonal pattern like in the diagram represented in Figure 1a. **Table 1** summarizes the main structural properties of the studied samples.

X-Ray Diffraction (XRD) analysis<sup>[12]</sup> revealed that Ni nanostructures were grown in face-centered cubic (fcc) polycrystalline nature with a (111) preferential orientation and with a calculated mean crystallite grain size of  $(50 \pm 5)$  nm for the Ni nanowire array sample and  $(21 \pm 3)$  nm for Ni 3DNNs.

It is worth noting that the relative volume ( $V_R$ ) of the TNWs represents only 2.6% of the Ni 3DNNs total volume for  $P = 445$  nm and 4.6% for  $P = 255$  nm. Even when the  $V_R$  values are below 5%, a high anisotropic magnetic response, depending on  $P$  or the separation between TNWs, has been observed.<sup>[12]</sup>

Regarding the magnetic characterization, we started our study by measuring the room temperature hysteresis loops (shown in **Figure 2**) and the first magnetization curves (see Figure S1 in the Supporting Information) with the external magnetic field applied at an angle  $\theta$  relative to the alumina template. Then,  $\theta$  was varied from  $0^\circ$  (in-plane configuration or perpendicular to the NWs longitudinal axis) to  $90^\circ$  (out-of-plane configuration or parallel to the NWs longitudinal axis). A scheme of the directions of the magnetic field applied with respect to the 3D nano networks is shown in Figure 2e. The in-plane (IP) and out-of-plane (OOP) measured coercivities ( $H_C^H$ ) and the reduced remanence values ( $M_r/M_s$ ) are reported in Figure 2d.

While the IP hysteresis loop of the Ni nanowire array (Figure 2a) shows the characteristic response of a hard magnetic axis with small coercivity and remanence, the easy magnetization axis is confirmed along the nanowire longitudinal axis (OOP or  $\theta = 90^\circ$ ). Although the magnetic response of a single Ni nanowire should be mainly governed by the shape anisotropy term, which favors the magnetization alignment along the nanowire axis. The magnetostatic interaction amongst nanowires has a strong contribution to the Ni nanowire array, resulting in a spontaneous demagnetization effect. This last term is responsible for reducing both coercivity and reduced remanence when nanoelements are densely packed, such as in this case, where the diameter/inter-wire distance ratio is 55/65.

On the other hand, the magnetic anisotropy in 3D Nano-Networks (3DNNs) is strongly modified by the presence of transversal nanowires (TNWs).<sup>[12]</sup> Hysteresis loops (Figure 2b,c) show that the easy magnetic axis evolves from parallel to the nanowire longitudinal axis for the Ni NW array to an almost isotropic behavior for the 3DNN with TNWs separated by 445 nm (3DNN445) or even perpendicular to the NW axis for TNWs separated by 255 nm (3DNN255). This fact is also confirmed by the angular dependence of the reduced remanence ( $M_r/M_s$ ) shown in Figure 2d). While  $M_r/M_s$  increases with  $\theta$  for the nanowire array and 3DNN445, it decreases for 3DNN255.

Both the nanowire array and the 3DNN445 sample show similar OOP  $H_C^H$  values and are larger compared to that of 3DNN255 (see Figure 2d). This is expected since the length of the nanowires affects the overall  $H_C^H$  due to the stray fields generated by magnetostatic interactions.<sup>[20]</sup> However, the IP  $H_C^H$  does not seem to follow any length or period ( $P$ ) dependence, and it presents a maximum value for the 3DNN445 sample. Regarding the reduced remanence values, the measured IP  $M_r/M_s$  increases significantly, up to 4-times the value observed for the Ni NWs, in the presence of the TNWs. In addition, the measured OOP  $M_r/M_s$  presents a more complex behavior with a maximum value for the 3DNN445 sample and a minimum for 3DNN255. Figure 2d) shows low  $M_r/M_s$  for all samples in any direction of the external applied magnetic field. This fact confirms that the magnetostatic interactions among NWs are demagnetizing, favoring the anti-parallel alignment and spontaneous demagnetization.

Both the resulting hysteresis loops (Figure 2) and first magnetization curves (Figure S1, Supporting Information) evidence that the TNWs and their periodicity modify dramatically the total anisotropy of the system. We hypothesize that behind these changes in the global magnetic properties, the special geometry of 3DNNs gives rise to atypical magnetostatic interactions among nanowires, which would decisively alter also the magnetization dynamics compared to the standard nanowire arrays. However, the hysteresis loops and first magnetization curves provide valuable but limited information about the magnetization behavior. They covered the evolution from opposite saturated states and from global demagnetized to saturated states. Nevertheless, accurate micromagnetic simulations and further validation by experimental FORC analysis can provide a deeper insight into the magnetic scenario, as it will be shown next.

Therefore, to discern the magnetization reversal process and obtain an accurate model of the effects generated by the TNWs, 3D micromagnetic simulations were first performed using MuMax3.10 software.<sup>[21]</sup> To reproduce the experimental results as accurately as possible, our models have simulated the nanostructures formed by the nanowire array shown in Figure 1a and with 4  $\mu$ m in length. We believe that this approach assures a significant and representative number



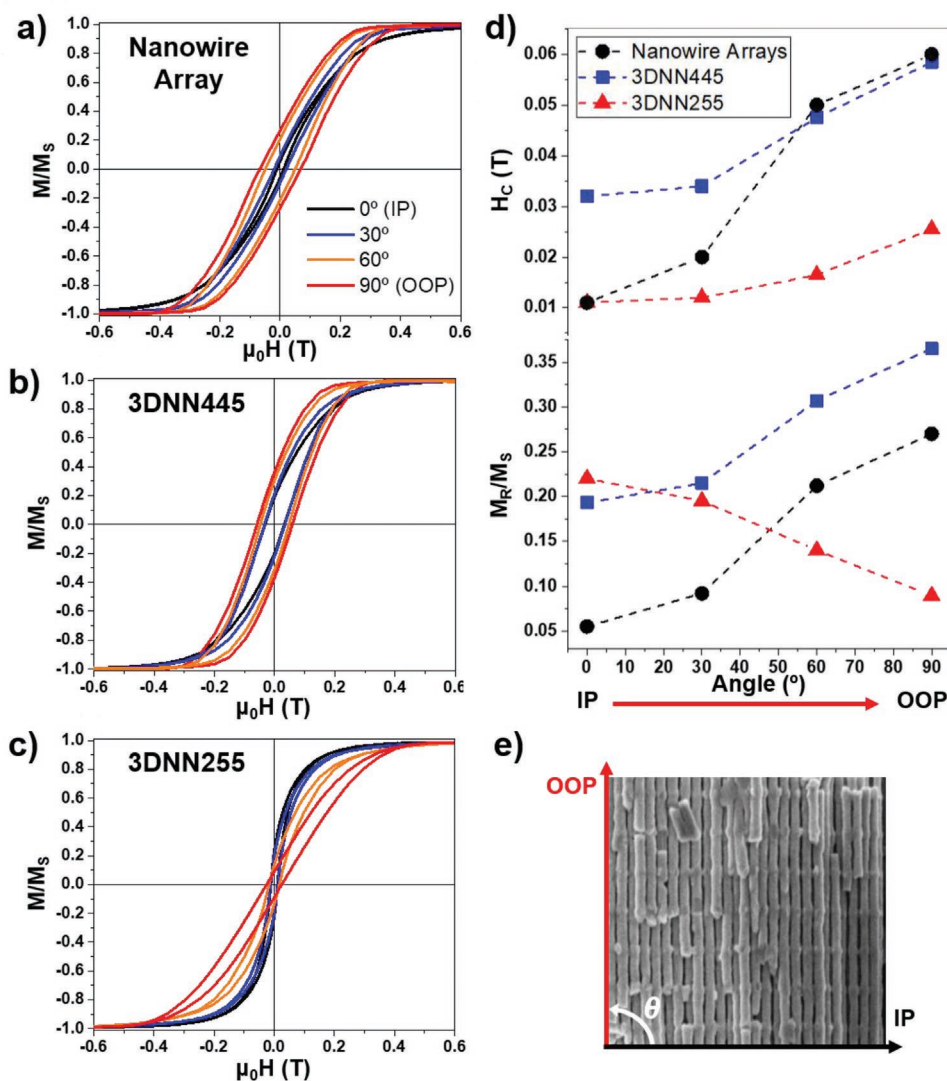


**Figure 2.** Hysteresis curves of a) Ni Nanowire array, b) 3DNN445, and c) 3DNN255. The black line corresponds to the IP ( $\theta = 0^\circ$ ), the red line to OOP ( $\theta = 90^\circ$ ), the blue line to  $\theta = 30^\circ$ , and an orange line to  $\theta = 60^\circ$ . d) Reduced remanence values ( $M_r/M_s$ ) and coercive fields ( $H_c^H$ ) as a function of  $\theta$  (The dash lines are a guide for the eye). e) A diagram, indicating the orientation of the applied external magnetic field.

of TNWs and NWs, albeit at the expense of computing time. Both the simulated first magnetization curves (Figure S2 in the Supporting Information) and simulated hysteresis loops (Figures 3–7) of the Ni nanowire arrays and 3DNNs have achieved good correlations with the experiments and thus provide a valid initial framework. However, we must recall that the observed deviations between the experimental results and the simulations are mainly due to the limited number of modeled elements and the exclusion of possible defects present in the samples. For instance, the jumps observed in the OOP hysteresis loops (see for example Figure 3c) have been associated with this limited number of modeled elements. In addition to the resulting global magnetization, these simulations provide a detailed evolution of the local magnetization states inside the nanowire array (See Figures 3a and 4a) as well as in the 3D NanoNetworks (Figures 5a and 6a; Videos S3–S7 in the Supporting Information).

To be able to go further in our analysis, FORC studies were also performed. Experimental FORC provides access to different magnetization states by multiple sequential minor hysteresis loops, beginning at different reversal fields ( $H_R$ ), and then evolving back to the positive saturation state. Based on the classical Preisach model, FORC analysis models the hysteresis as a set of independent irreversible processes known as hysterons.<sup>[22]</sup> Each hysteron is characterized by its coercivity,  $H_c^F$ , and a bias or interaction field  $H_U$ . Ideally, FORC analysis is an interesting and powerful characterization tool as hysterons provide statistical information about the reversible and irreversible processes.<sup>[23]</sup> However, we should remark that extracting information on the intrinsic properties of a material from FORC measurements is a not trivial and complicated process. In particular, the general Preisach model, with unit magnetization based on hysterons, provides an incomplete model for interacting nanostructures,

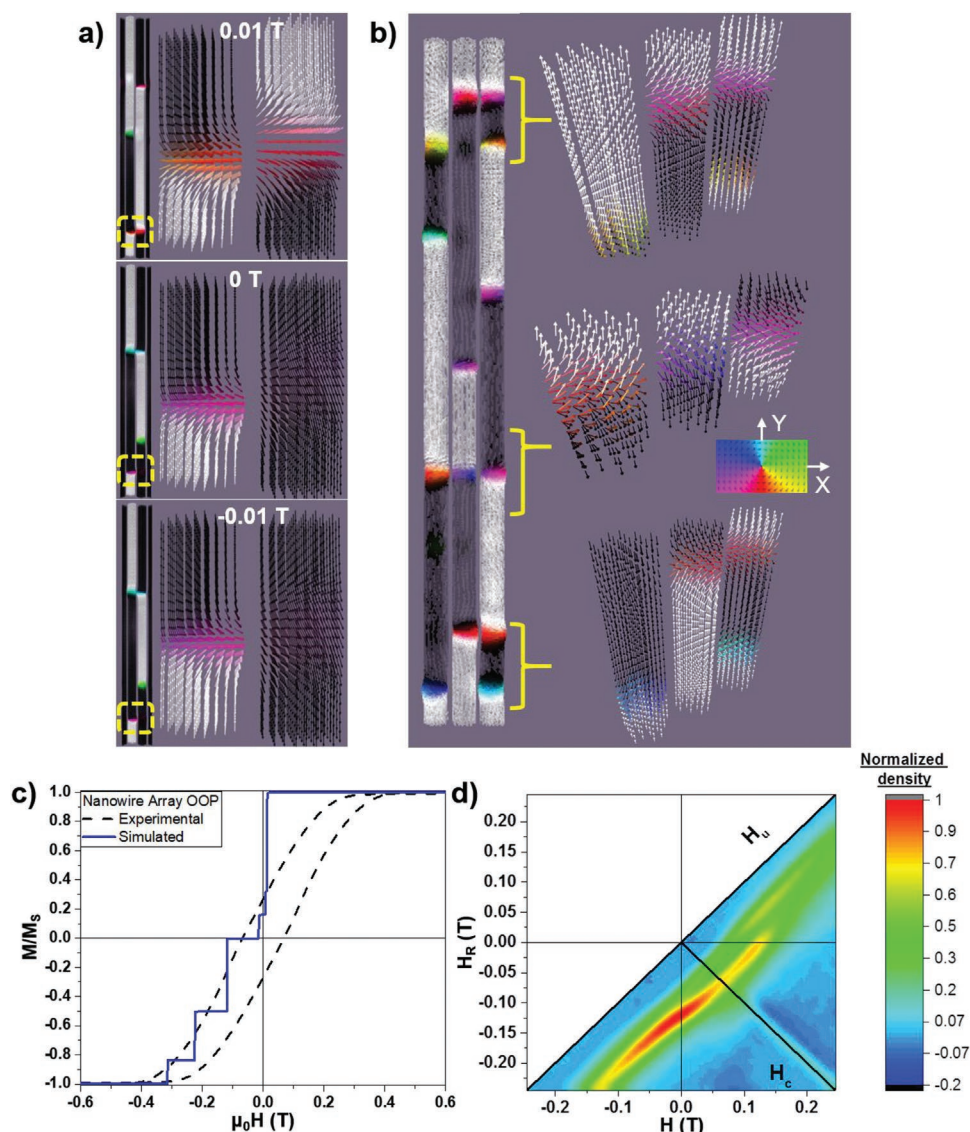


**Figure 3.** a) Simulated OOP magnetization reversal of the Ni nanowire array. The figure highlights the interactions and pinning of DWs. For each panel on the left side, two NWs are represented. The yellow squares on the left panels denote the zones that have been magnified on the right side of the images. b) Simulated nanowire array at the demagnetized state. The left side shows the complete cross-section view of 3 NWs, and on the right side, detailed views of the DW configuration from those zones are denoted by the yellow brackets. c) Experimental and simulated OOP hysteresis loop and d) OOP FORC diagram.

due to the complex interplay between the dipolar and exchange couplings as well as the distribution of intrinsic coercivity fields due to element size, defects, or any other inhomogeneity.<sup>[24]</sup>

The FORC distribution  $\rho$  is calculated through a second-order mixed derivative of magnetization,  $M$ , for the externally applied field ( $H$ ) and the reversal field ( $H_R$ ):<sup>[25]</sup>

$$\rho(H, H_R) = -\frac{1}{2} \frac{\partial^2 M}{\partial H \partial H_R} (H \geq H_R) \quad (1)$$

Apart from the main coordinate system,  $H_R$  &  $H$ , our FORC distributions also show a secondary coordinate system that essentially consists of the local coercivity ( $H_C^E$ ) and the interaction field ( $H_U$ ). The transformation from  $(H, H_R)$  coordinates is accomplished by a 45° rotation and using:

$$H_C^E = \frac{H - H_R}{2} \quad \text{and} \quad H_U = \frac{H + H_R}{2} \quad (2)$$

The resulting FORC diagrams for OOP and IP orientations are presented in Figures 3–7 in context with the micromagnetic simulations. The OOP FORC diagrams share some common features such as an elongated distribution along  $H_U$  axis due to the intense dipolar interactions ( $\geq 0.2$  T) among the densely packed nanowires (diameter/inter-wire distance ratio = 55/65). However, FORC diagrams also showed a striking behavior in the presence of TNWs with a notable evolution from the nanowires arrays to the 3DNN samples and depending on the periodicity ( $P$ ). To simplify the analysis and discussion of our results, we will present first the results for the nanowire arrays in the OOP and IP configurations. Then, since the most dramatic

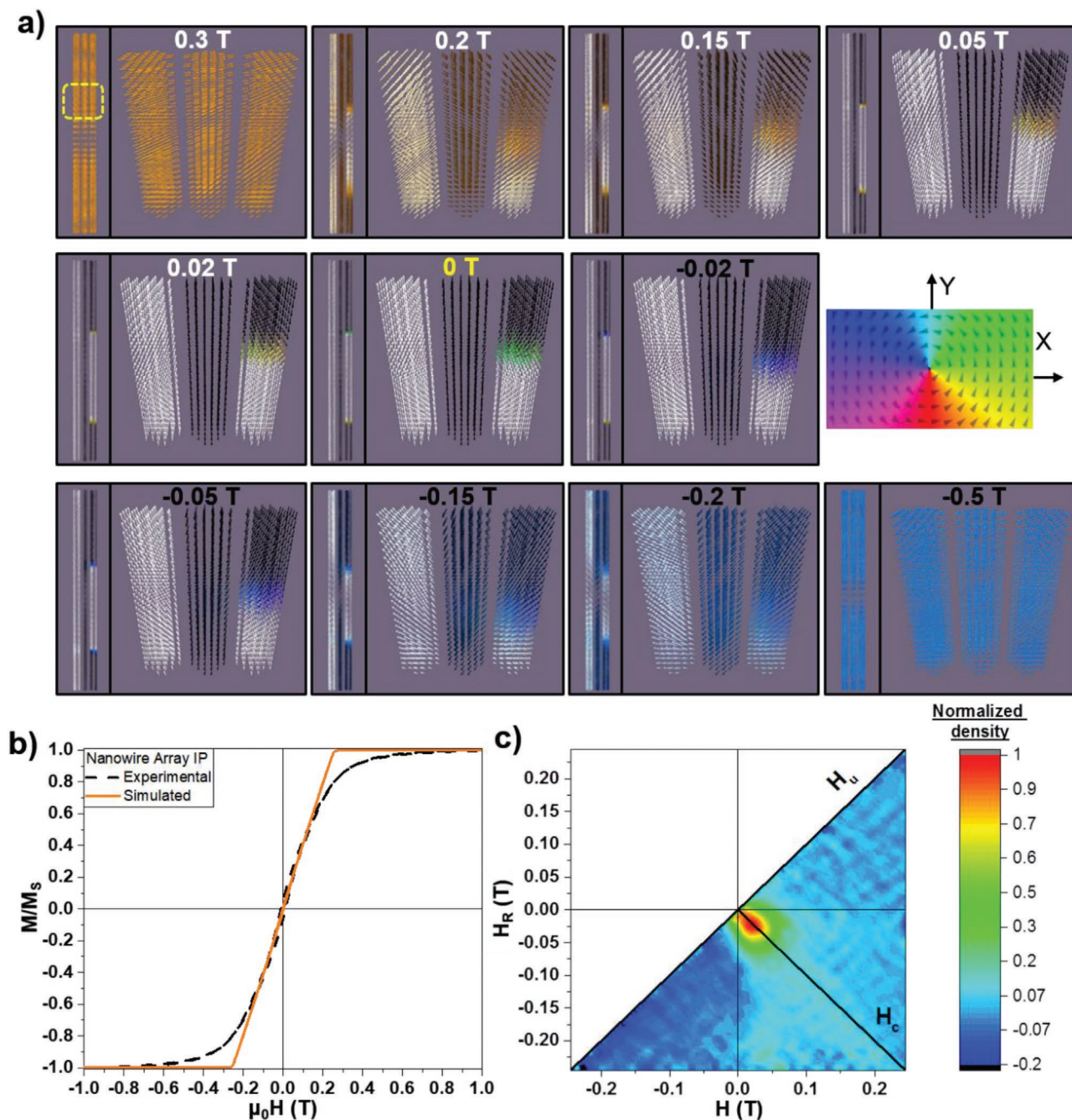


**Figure 4.** a) Simulated IP magnetization reversal of Ni NWs. A yellow square on the left panel denotes the magnified areas on the right side. b) Simulated and experimental IP hysteresis loops. c) IP FORC diagram.

changes rise for the 3DNN255 sample, we will follow with the OOP response of 3DNN255 and 3DNN445, and continue with their IP configurations.

As was described in the literature,<sup>[23]</sup> the OOP FORC diagram of the Ni nanowire array (Figure 3d) presents a T-shape structure with an elongated distribution along  $H_u$  axis, or interaction field distribution (IFD), with an interaction field value at saturation  $>0.2$  T, and a less prominent ridge along the coercive field axis ( $H_c$ ) or the coercive field distribution (CFD).<sup>[24a-c]</sup> While IFD in nanowire arrays is

usually related to the switching of the nanowires with small intrinsic coercive fields and under the existence of strong demagnetizing field interactions, CFD is generated by the nanowires with the largest coercive fields.<sup>[24a-c]</sup> In this case, the FORC distribution, shown in Figure 3d), suggests a left-shift of the main signal while reducing the reversal field to a more negative value. This behavior together with the presence of weak negative tails is a clear sign of strong demagnetizing interaction.<sup>[24d,26]</sup> It is in good agreement with the expected strong dipolar interactions that were confirmed by



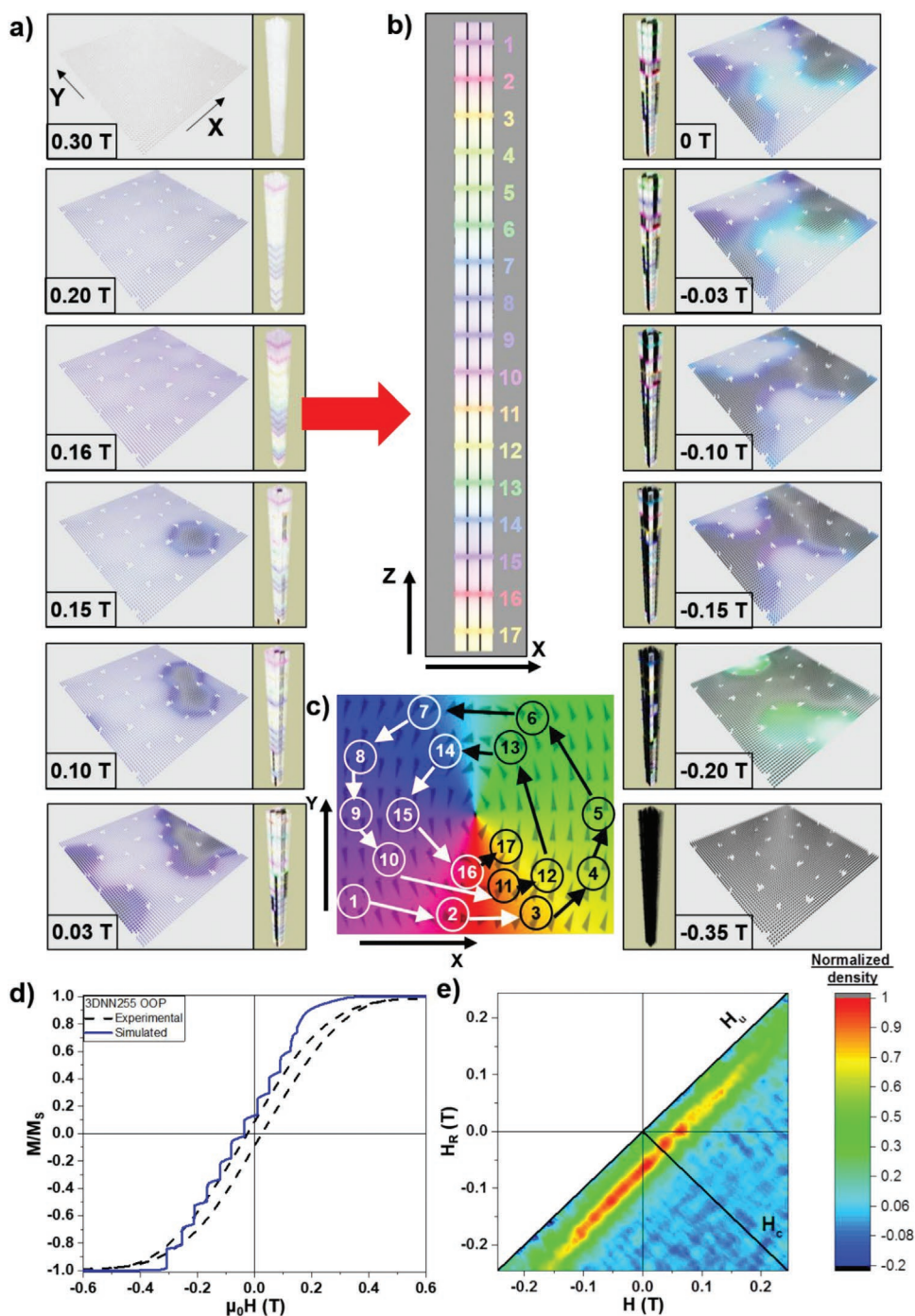


**Figure 5.** Simulated OOP magnetization reversal sequence of 3DNN255. a) Each panel shows the dependence of the magnetic configuration with the externally applied field and it is composed of a 3D view of the whole sample and the top-view ( $XY$  plane) of the 9th TNW level. b) The cross-section view ( $XZ$  plane) of the whole sample at  $H = 0.16$  T (pointed with a red arrow) is represented at the center of the figure showing the TNW corkscrew configuration. c) Color map (magnetization direction) where each number relates each TNW level with its predominant magnetization direction at corkscrew configuration. d) Experimental and simulated OOP hysteresis loops. e) OOP FORC diagram.

the hysteresis loops and observed also in the micromagnetic simulations (see below).

In addition, we should note that 2 different local maxima or irreversible processes are detected in Figure 3d). The most intense peak is located at  $H = -0.01$  T and  $H_R = -0.125$  T ( $H_C^F = 0.06$  T and  $H_U = -0.065$  T), while the weak one is at

$H = 0.135$  T and  $H_R = 0.06$  T ( $H_C^F = 0.04$  T and  $H_U = 0.0875$  T). FORC distributions with similar shapes and multiple peaks in the IFD have been already reported for highly interacting long ( $L = 30$   $\mu\text{m}$ ) Fe nanowires,<sup>[27]</sup> as well as in bi-segmented Ni/Co NW Arrays.<sup>[28]</sup> In this last publication, it was claimed that one peak is related to the magnetization reversal of the

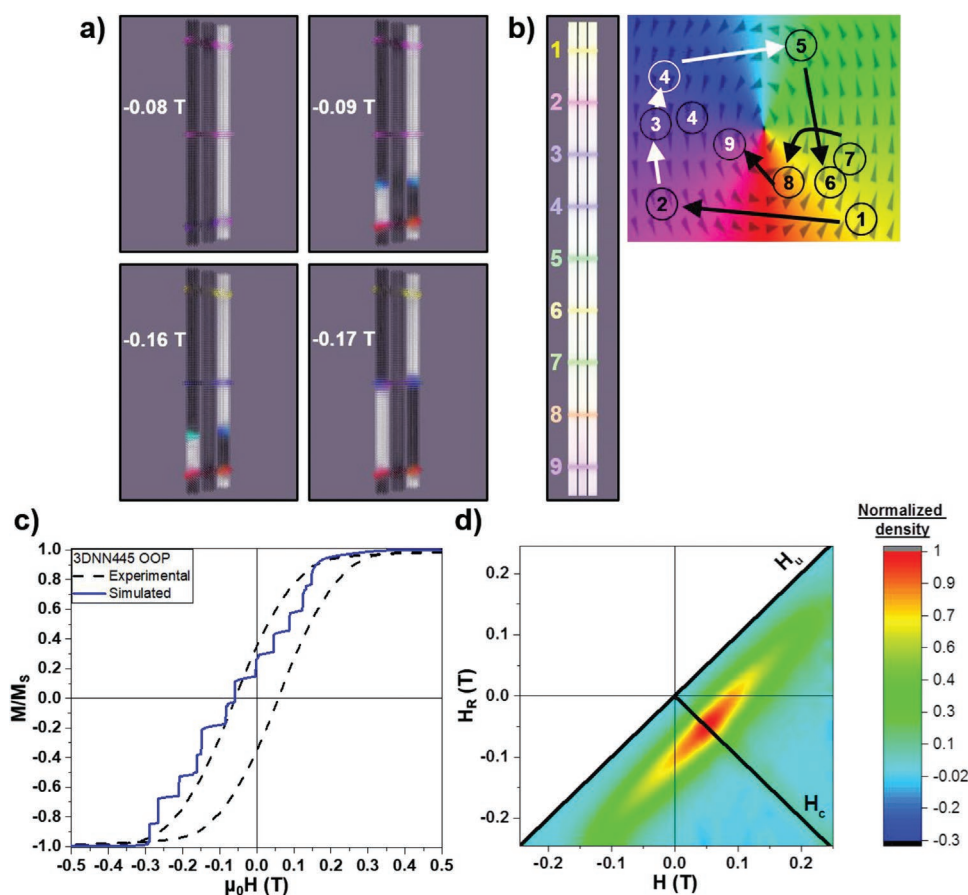


**Figure 6.** a) Cross-section images of the simulated OOP magnetization reversal of 3DNN445 as a function of the external applied magnetic field. b) The cross-section view ( $XZ$  plane) of the whole sample at  $H = 0.20$  T and showing the IP configuration of the TNW levels. Each level is denoted by a colored number that relates to the numbers in the color map (magnetic direction) on the right hand. c) Experimental and simulated OOP hysteresis loops. d) OOP FORC diagram.

whole bi-segmented Ni/Co NW. The second one is caused by the magnetization reversal of only the Ni segment while the Co segment in some NWs is magnetized antiparallel. Finally, the third peak links to the switch back of the Ni portion of the Ni/Co NWs that was aligned antiparallel and thus, the Ni and Co segments become parallel again.

On the other hand, the reported OOP micromagnetic simulations of NWs<sup>[29]</sup> have demonstrated that the reversal mode corresponds to the nucleation and propagation of a domain wall from the NW extremities. In particular, Ni NWs with a diameter  $\geq 40$  nm show the nucleation and propagation of domain walls in vortex configuration.<sup>[29]</sup> Our simulations confirm also that the magnetization reversal process is driven by the nucleation and propagation of domain walls. However, in opposition to what has been usually reported, we have observed that multiple transverse domain walls have been nucleated (see Figure 3a) and these transverse domain walls interact with neighboring NWs, even acting as pinning centers. Then, NWs divide in magnetic multi-domains during the magnetization reversal and this behavior was also confirmed at the demagnetized state (shown in Figure 3b). This segmentation in multi-domains was previously predicted by the  $M_R/M_S$  values extracted from the experimental hysteresis loops.

Based on the experimental results and supported by our micromagnetic simulations (Figure 3; Video S3, Supporting Information) we suggest that the weak peak corresponds to the spontaneous reversal of a few nanowires under the effect of the magnetostatic interactions, while the intense irreversible feature is associated with the nucleation-propagation of domain walls during the reversal process of the multi-domains NWs.

When the external magnetic field was applied perpendicular to the wire axis, i.e., along the hard magnetization axis, Figure 4c shows a single reversal event centered at  $H_C^F = 0.0250$  T and with an interaction field value at saturation of  $\approx 0.0300$  T that is considerably smaller than the values observed in the OOP direction. This signal moves toward larger fields ( $H$ ) while reducing the initial reversal fields ( $H_R$ ) suggesting that nanowires are under the influence of positive ferromagnetic-like interactions. This tends to promote the stability of the initial reversed condition<sup>[24d,26]</sup> and it is also confirmed by the large and weak negative tail. Then, the IP FORC diagram of the Ni nanowire array (Figure 4c) is consistent with the results reported in the literature,<sup>[23b,d,30]</sup> where a nearly reversible magnetization process by coherent rotation has been suggested. But, if the IP magnetization reversal of a NW should be achieved by a pure coherent rotation (a reversible process), no



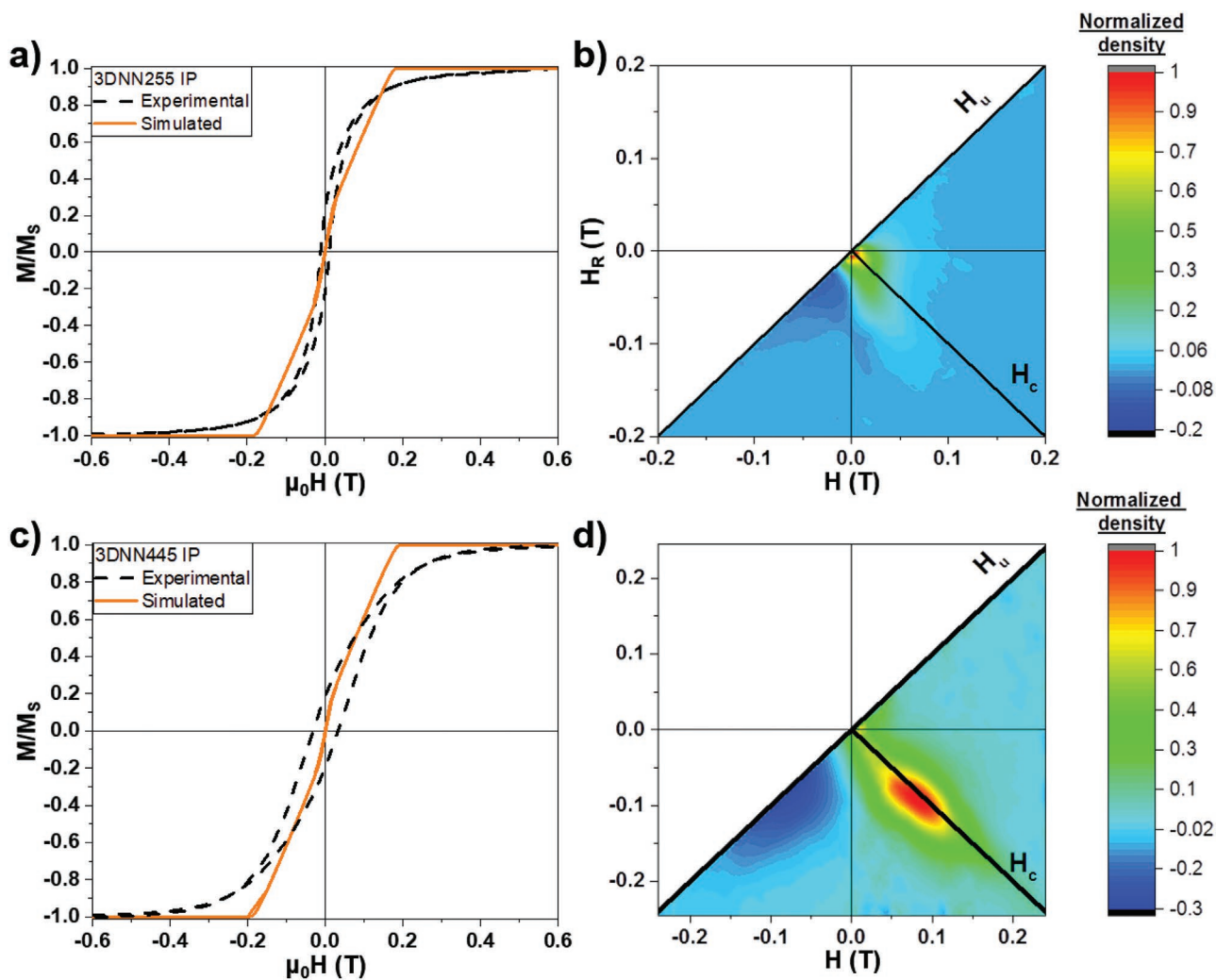


**Figure 7.** a) Experimental and simulated IP hysteresis loop and b) IP FORC diagram of sample 3DNN255. c) Experimental and simulated IP hysteresis loops and d) IP FORC diagram of sample 3DNN445.

irreversible features are expected in the FORC diagrams. Then, other mechanisms must be considered to justify the observed peak. For example, the magnetization reversal of the NWs and/or the nucleation of closure domains at the nanowire extremities have been already suggested as possibly responsible for the appearance of irreversible features.<sup>[23b,d,30]</sup>

Regarding the IP simulations, Figure 4a confirms that the magnetization reversal process is mainly driven by coherent rotation. As it was described for the OOP configuration, NWs also split into magnetic domains, separated by domain walls but these DWs in the IP geometry stand and do not propagate along the NW with the external applied magnetic field. Then, simulations suggest that the observed feature in Figure 4d is related to the presence of these DWs. For instance, we suggest that the reversible distribution corresponds to the coherent rotation of the domains, while the irreversible one, observed at  $H_C^F = 0.025$  T, reflects the generation/annihilation of DWs.

Next, we focus our attention on the Ni 3DNNs and we analyze first the system with the shorter periodicity ( $P = 255$  nm) between TNWs (3DNN255). Its OOP FORC distribution

(Figure 5e), instead of a T-shape, presents an elongated shape along  $H_U$ , with a much flatter profile, and the distribution has noticeably shifted to a lower value, which now is located at  $H_C^F = 0.0325$  T. The shape of the distribution along the interaction field axis (IFD) can constitute a criterion to distinguish the interaction regime acting over the sample.<sup>[24c]</sup> In particular, when we are considering an array of ferromagnetic entities, such as our nanowire arrays, the total magnetic field acting on each wire is the sum of the external applied magnetic field and the magnetostatic dipolar field. While the first term is homogeneous along the whole sample, the homogeneity of the second contribution depends on the sample. For example, the different magnetostatic dipolar fields among NWs located at the center of the nanowire array or the sample extremities, known as border effects, contribute to such inhomogeneity. Therefore, the shape of the distribution along the interaction field axis (IFD) can be used to estimate the magnetic field homogeneity acting on the sample.<sup>[24c]</sup> When this profile shows a peak, as discussed for the nanowire array, the sample is subjected to the presence of inhomogeneous dipolar magnetic interactions, in opposition to

the generation of a homogeneous field exhibiting an IFD flat profile.

Regarding the OOP micromagnetic simulations of 3DNN255 (Figure 5 and full sequence in Video S4 in the Supporting Information), the OOP magnetization reversal begins from the OOP saturated state (white arrows in our case). When the external magnetic field was reduced, TNWs start to rotate their magnetization to the IP configuration, meanwhile, the NW segments (or the NW limited by two TNWs, see Figure 1) keep their magnetization OOP (Figure 5a) with  $H_{\text{ext}} = 0.16$  T). At this point, we observe that the IP magnetization at each TNW level is homogeneous, with all magnetic moments pointing in one direction. Although this direction is different for each level, we must emphasize that the magnetization direction at these levels is not random and shows an in-plane rotation from one TNW level to the next one. Then, the IP magnetization at the TNW levels adopts a corkscrew-like configuration along the longitudinal NWs axes (see the central panel in Figure 5b) confirming the presence of a significant magnetostatic coupling between the TNW levels. By continuing to reduce the externally applied magnetic field, the magnetization of the NWs segments rotates from OOP to the IP configuration at the intersection between the NWs segments and TNWs, while, the central parts of the NW segments keep the OOP orientation. This stage remains until the OOP magnetization reversal of some NWs segments is abruptly achieved. Contrary to what is usually observed in ferromagnetic NWs, where the OOP reversal process starts at the NWs extremities, this event occurs starting from the NWs segments/TNWs intersections and the full magnetization reversal can be achieved in segments located anywhere along the NW and in any wire of the array (Figure 5).

The complexity of the magnetization reversal process can be directly linked to its related FORC diagram. In particular, it is claimed that our OOP FORC distribution, elongated along the  $H_U$  axis (Figure 5d), is formed by multiple overlapping peaks. These peaks correspond to multiple switching events that occur even when the homogeneity of the magnetostatic interaction field was significantly improved by the TNWs. Then, we conclude that the irreversible events correspond to the complete magnetization reversal of the NW segments located anywhere along the NW and in any wire of the array.

Now, we analyze the OOP case when the TNW period ( $P$ ) increases to 445 nm. As for the nanowire array, the OOP FORC distribution of 3DNN445 (Figure 6d) presents a T-shape structure with an elongated distribution along the  $H_U$  axis (IFD) and a less prominent ridge along the coercive field axis (CFD), denoting a switching field distribution interacting with a demagnetizing interaction field.<sup>[24b]</sup> A single peak is located at  $H = 0.05$  T and  $H_R = -0.05$  T ( $H_C^F = 0.052$  T and centered on the  $H_U$  axis). Similar OOP FORC distributions have been reported for shorter and less interacting nanowire arrays.<sup>[23c,f-h,31]</sup>

The OOP easy magnetization axis, determined from the hysteresis loops (shown in Figure 2b), in combination with the T-shape structure of the OOP FORC distribution (Figure 6d), point out that we are facing a magnetic behavior similar to like that previously described for the Ni nanowire arrays. This means that the NWs segments, or at least some of them, in 3DNN445 are long enough to sustain their division in magnetic domains during the magnetization reversal. Although the OOP

micromagnetic simulations of 3DNN445 (Figure 6 and full sequence in Video S5 in the Supporting Information) reveal a magnetization reversal mechanism similar to that of sample 3DNN255, the breaking in magnetic domains of the NWs segments is also corroborated. Then, the 3DNN445 magnetization reversal should be described by a hybrid process between those of nanowire arrays and 3DNN255. In addition, the corkscrew-like configuration of the IP magnetization at the TNW levels is not as evident as in the 3DNN255 sample, confirming that the magnetostatic coupling between adjacent TNW levels is reduced when  $P$  increases from 255 to 445 nm.

The IP magnetic responses of 3DNNs (see Figure 7b,d) show diagrams that are the ones observed for the nanowire array (shown in Figure 4c). Again, there is a single reversal event moving to larger fields ( $H$ ) when the reversal fields ( $H_R$ ) were reduced, as well as a large negative tail (particularly visible for 3DNN455), suggesting the existence of positive magnetizing exchange interactions among nanowires. However, the 3D nano-networks also exhibit some peculiarities. The IP FORC distribution of 3DNN255 (Figure 7b) presents an intense peak at  $H_C^F = 0.0050$  T and a lobe through  $H_C^F$  and negative  $H_U$  axes. This type of lobe has been observed neither in the nanowire arrays nor in 3DNN445 (described below), but it was previously reported in a Ni antidot array under the influence of non-cylindrical Ni nanopillars,<sup>[32]</sup> Fe regular antidots<sup>[33]</sup> as well as in an artificial spin ice system.<sup>[34]</sup> Usually, this lobe, also called the “left-bending boomerang”, points out the nucleation and abrupt propagation of domain walls.<sup>[34]</sup> This mechanism is compatible with the IP magnetization reversal of 3DNN255 obtained by the micromagnetic simulations (full sequence shown in Video S6 in the Supporting Information). When the IP magnetic field was reduced from the saturation field, the magnetization of the NW's segments, mainly placed at the center of the sample, switch to the OOP configuration; meanwhile, TNWs maintain their IP magnetization. This OOP rotation begins at the middle of the segments and propagates toward the interconnections between NWs and TNWs. A larger reduction of the applied magnetic field initiates the IP magnetization rotation along the field direction of the TNWs. However, part of the TNW suffers an abrupt IP magnetization reversal at low fields, followed by the IP magnetization rotation of the segments until the whole sample is fully saturated.

Therefore, this simulated magnetization reversal process is compatible with the measured IP FORC for 3DNN255 (Figure 7b). The FORC distribution observed at low  $H_C$  and  $H_U$  is related to the magnetization reversal of the NW segments. Meanwhile, the observed lobe could be related to the abrupt IP magnetization reversal stage of the TNW combined with the segments.

When  $P$  increases to 445 nm (3DNN445), the IP magnetic response diverges markedly from that of the shorter period. The IP FORC diagram of 3DNN445 (Figure 7d) presents an irreversible peak which is mainly located along the  $H_C$  axis and has shifted up to  $H_C^F = 0.0845$  T. Like in the nanowire arrays, this peak confirms an interaction field value of  $\approx 0.03$  T, but the distribution is broader along the coercive field axis ( $>0.06$  T) meaning a broad population of coercivities or switching events.

Contrary to the results obtained from the IP micromagnetic simulations of the Ni nanowire array and 3DNN255, the IP

simulations of 3DNN445 (Video S7 in the Supporting Information) suggest that each NWs segment is fully magnetized, segments are not broken into magnetic domains, and magnetization point to the any of the OOP directions during the reversal process. Consequently, the broad distribution in the FORC diagram (Figure 7d), at high  $H_C$ , must be related to the irreversible process that is the magnetization reversal of the NWs segments. In addition, the broader distribution along the coercive field axis is justified by the fact that the magnetization switching of the NWs segments occurs throughout the whole magnetization reversal process of the sample and as long as the sample is not saturated.

### 3. Summary

This methodology allows the synthesis of a new generation of scalable magnetic nanostructures with precise control of both the position and number of TNWs. The work demonstrates that large areas (up to a few  $\text{mm}^2$ ) of Ni nanowires arrays interconnected through transversal nanowires (TNWs) give rise to unexpected magnetization responses, which radically evolve depending on the TNW arrangement.

We propose a magnetic framework, where the main magnetic features have been cross-verified by hysteresis loops, first magnetization curves, FORC and micromagnetic simulations. In this scenario, TNWs play a capital role and give rise to a complex landscape of magnetic behavior within the Ni 3D Nano-Networks (3DNNs). Our results confirm that TNWs behave like pinning sites for the magnetic domain walls and reduce the magnetostatic interactions among NWs. In particular, we have observed that TNWs contribute to the global homogeneity of the magnetostatic dipolar field acting over the sample and that this contribution improves when the separation between TNW levels ( $P$ ) is reduced.

In the OOP configuration, TNWs control the effective length for the generation of multiple magnetic domains along a nanowire. NW segments are monodomains and TNWs behave like good pinning sites for the magnetic domain walls when  $P$  is short enough, like in 3DNN255. Larger  $P$  are not efficient for the correct pinning of DWs and the NW segments split in multidomains, like in 3DNN445 and as was previously described for the Ni nanowire array. Even more, our model predicts the generation of a particular global ordered magnetization state (corkscrew-like state) during magnetization reversal for 3DNN255. This state is worse defined for larger  $P$  (3DNN445).

Although the coherent rotation is the common magnetization reversal mechanism for nanowire arrays and 3DNNs in the IP configuration, it was demonstrated that the nucleation or formation of DWs can occur at any point along any nanowire in the Ni nanowire arrays, as well as at the center of the NW segments in 3DNN255. On the other hand, the IP magnetization reversal of 3DNN445 is mainly reached after passing through the OOP magnetization reversal of the NWs segments.

We believe that the obtained results provide a deeper understanding of the magnetic behavior of these novel nanostructures with well-controlled and tuned magnetic properties through the introduction of several levels/periods of TNWs. Moreover, the validated framework of magnetization dynamics,

based on the generation/annihilation and interaction of DWs, in these self-ordered systems, represents a useful tool that will enable the design of high-resolution 3D magnetic nanonetworks. The presented experimental and modeling results pave the way for controlling DWs in new ways of logic computation and sensing or even for the future designing a-la-carte of magnetic metamaterials by the combination of different materials and/or periods within the same 3D nanonetwork.

### 4. Experimental Section

**Sample Fabrication:** 3D nanowire networks were fabricated via template-assisted electrochemical deposition. The templates used were anodic aluminum oxide (AAO) produced following the technique described in Reference,<sup>[5c]</sup> which consists of a two-step anodization process in a sulfuric acid solution (0.3 M  $\text{H}_2\text{SO}_4$  at 0 °C). While the first anodization step defines the order of the nanopores (at a constant voltage of 25 V), the second one controls the pore lengths. In addition, a pulsed voltage process was applied during the second anodization step to alternate between mild and hard anodization (at 25 and 32 V, respectively). Afterward, a chemical etching of the AAOs was performed using a phosphoric acid solution (5% wt.  $\text{H}_3\text{PO}_4$  at 30 °C for  $\approx 25$  min for AAO thicknesses of 30  $\mu\text{m}$ ). As the chemical etching has different rates for the mild and hard anodized regions, the final structure consists of nanopores of around 50 nm in diameter with an inter-wire distance of 65 nm and interconnected with a net of perpendicular nanopores of around 30 nm in diameter. These connecting nanopores are formed in the areas corresponding to the hard anodization, and thus the distance between consecutive planes of connecting nanopores can be fine-tuned by changing the pulses in the second anodization step. In such a way, 3D-AAOs with different periods ( $P$ ) between the planes of transversal pores were fabricated with pulses of 180 and 270 s, which correspond to a  $P$  of 255 and 455 nm, respectively.

A 5 nm thick Cr layer plus a 150 nm thick Au layer were evaporated on one side of the 3D-AAOs and it was used as the working electrode for a three-electrode electrochemical deposition where Ag/AgCl (saturated KCl) was the reference electrode and a platinum mesh as the counter electrode. The electrochemical bath used for Nickel deposition was 0.75 M  $\text{NiSO}_4 \cdot 6\text{H}_2\text{O}$ , 0.02 M  $\text{NiCl}_2 \cdot 6\text{H}_2\text{O}$ , and 0.4 M  $\text{H}_3\text{BO}_3$ . The pulsed electrodepositions were realized during the on-time at  $-0.9$  V versus Ag/AgCl at 45 °C for 1 s and for the off-time of 0.1 s (with no current applied) to obtain a homogenous growth front with a high filling ratio. In such a way, Ni 3D nanowire networks (Ni 3DNNs) were grown with two different spacing between the transversal nanowires: 255 and 445 nm (named in this work as 3DNN255 and 3DNN445, respectively). 1D Ni nanowire arrays were also fabricated in porous alumina using similar conditions.

**Morphological and Crystallographic Characterization:** SEM images were taken with a high-resolution scanning electron microscope (HRSEM, FEI Verios 460). The crystalline orientation was measured with an X-Ray diffractometer Philips X'Pert PANalytical four circles diffractometer, with a  $\text{Cu K}\alpha$  wavelength of 0.15418 nm. The electron tomography experiments were conducted in samples once the alumina matrix was dissolved and the samples were broken into smaller pieces by sonication and dispersed in ethanol. A Thermofisher Titan Themis operated at 200 keV was used to obtain the set of high angle annular dark-field (HAADF) images used for the reconstruction. The angular range for this tilting experiment was  $\pm 65^\circ$ , acquiring a single projection image each  $5^\circ$  (up to a total of 25 images). An implementation of a TV minimization algorithm (TVAL3),<sup>[35]</sup> ran in Matlab, was used to resolve the reconstruction problem.<sup>[36]</sup> The alignment of the projections before the reconstruction step was carried out using the Thermofisher Inspect 3D (proprietary software) and the TomoJ plugin of the ImageJ (free software). The inspection of the reconstructed volumes, and visualization, were carried out in the Thermofisher Avizo software (proprietary).



**Magnetic Measurements:** Room temperature hysteresis loops, first magnetization curves, and FORC diagrams were measured in a vibrating sample magnetometer (VSM, model Microsense EZ-7). Previously to the measurement of the First Magnetization curves, samples were submitted to a demagnetization process using a saturation field of 1.5 T. These processes were applied for all configurations. FORC diagram precision is governed by the magnetic field and reversal field steps,  $H$  and  $H_R$ , respectively. In this work, the acquisition covered  $\pm 0.25$  T region, and 100 reversal curves were performed with 0.0050 T field spacing and a saturating magnetic field of 1.6 T. The data treatment was performed by Matlab code and Hysersoft<sup>[37]</sup> software.

**Micromagnetic Simulations:** Micromagnetic simulations at 0 K were performed using MuMax3.10 software.<sup>[21]</sup> Based on the morphological analysis of our samples (shown in Figure 1) and computational limitations, the nanostructure described in Figure 1a was modeled using nanowires with 55 nm of diameter, 4  $\mu\text{m}$  of length, and distributed in a hexagonal compact packed (*hcp*) configuration with a center-to-center NW distance of 65 nm. Next, 3DNNs were simulated by adding TNWs distributed in levels that have been separated by 240 and 450 nm for 3DNN255 and 3DNN445, respectively. Regarding the magnetic parameters, the standard values for the micromagnetic simulation of Ni NWs were used such as a magneto-crystalline anisotropy constant of  $K_C = -4.8 \times 10^4 \text{ erg cm}^{-3}$ , an exchange stiffness constant of  $A = 3.4 \times 10^{-7} \text{ erg cm}^{-1}$ , and a magnetization value of  $M_S = 490 \text{ emu cm}^{-3}$ .<sup>[38]</sup> In addition, random 3D Voronoi tessellation was implemented to emulate the size effect of the crystalline grains in the nanostructures. The grain sizes were chosen according to those obtained from the XRD analysis. Then, the exchange coupling constant between grains was settled to be reduced by 10%, while the  $K_C$  value of each grain was settled to be randomly varied up to 10% of the Ni magneto-crystalline anisotropy constant. As the Ni exchange length is  $l_{\text{ex}} \approx 4.8 \text{ nm}$ , the cell size was chosen to be  $(3 \times 3 \times 4) \text{ nm}^3$ . Periodic Boundary Conditions (PBC) in the sample plane were always included in our simulations. On the other hand, PBC along the nanowire axis, or the out-of-plane direction, were used for the Ni nanowire array. However, it was decided to not use PBC along the nanowire axis because no significant differences were observed in the simulations performed with and without them. As the steepest conjugate gradient method to minimize the total energy was used (MINIMIZE function), the damping parameter was taken as 0.5 to ensure rapid convergence. The RK45 or Dormand–Prince was the employed solver in our simulations.

## Supporting Information

Supporting Information is available from the Wiley Online Library or from the author.

## Acknowledgements

M.M.G. and O.C.C. acknowledge the financial support from the project PID2020-118430GB-I00 (MICINN). J.B.P., and F.P. acknowledge the financial support from PID2019-106165GB-C21 (MICINN) and M. López-Haro and J.J. Calvino from the University of Cádiz for the acquisition of the electron tomography series. The authors also acknowledge the service from the X-SEM Laboratory at IMM, and funding from MINECO under project CSIC13-4E-1794 with support from the EU (FEDER, FSE). The authors acknowledge the support for simulation hardware from J.L. Mesa at INTA. D.N. acknowledges the financial support from the project PID2019-108075RB-C31 and the grant RYC-2017-22820 funded by MICINN/10.13039/501100011033 and by “ESF Investing in your future”.

## Conflict of Interest

The authors declare no conflict of interest.

## Data Availability Statement

The data that support the findings of this study are available from the corresponding author upon reasonable request.

## Keywords

3D magnetic nanostructures, First Order Reverse Curves (FORC), metamaterials, micromagnetic simulations

Received: May 3, 2022

Revised: May 31, 2022

Published online:

- [1] a) A. Fernández-Pacheco, R. Streubel, O. Fruchart, R. Hertel, P. Fischer, R. P. Cowburn, *Nat. Commun.* **2017**, *8*, 15756; b) P. Fischer, D. Sanz-Hernández, R. Streubel, A. Fernández-Pacheco, *APL Mater.* **2020**, *8*, 010701.
- [2] a) J. De Teresa, A. Fernández-Pacheco, R. Córdoba, L. Serrano-Ramón, S. Sangiao, M. R. Ibarra, *J. Phys. D: Appl. Phys.* **2016**, *49*, 243003; b) A. Fernández-Pacheco, L. Skoric, J. M. De Teresa, J. Pablo-Navarro, M. Huth, O. V. Dobrovolskiy, *Materials* **2020**, *13*, 3774; c) I. Utke, P. Hoffmann, J. Melngailis, *J. Vac. Sci. Technol., B: Microelectron. Nanometer Struct. –Process., Meas., Phenom.* **2008**, *26*, 1197.
- [3] R. Winkler, B. B. Lewis, J. D. Fowlkes, P. D. Rack, H. Plank, *ACS Appl. Nano Mater.* **2018**, *1*, 1014.
- [4] a) C. Donnelly, M. Guizar-Sicairos, V. Scagnoli, M. Holler, T. Huthwelker, A. Menzel, I. Vartiainen, E. Müller, E. Kirk, S. Gliga, *Phys. Rev. Lett.* **2015**, *114*, 115501; b) G. Williams, M. Hunt, B. Boehm, A. May, M. Taverne, D. Ho, S. Giblin, D. Read, J. Rarity, R. Allenspach, *Nano Res.* **2018**, *11*, 845.
- [5] a) S. Vignolini, N. A. Yufa, P. S. Cunha, S. Guldin, I. Rushkin, M. Stefić, K. Hur, U. Wiesner, J. J. Baumberg, U. Steiner, *Adv. Mater.* **2012**, *24*, OP23; b) L. Yu, Z. Yan, H.-C. Yang, X. Chai, B. Li, S. Moeendarbari, Y. Hao, D. Zhang, G. Feng, P. Han, *IEEE Magn. Lett.* **2016**, *8*, 1; c) J. Martín, M. Martín-González, J. F. Fernández, O. Caballero-Calero, *Nat. Commun.* **2014**, *5*, 5130.
- [6] A. Ruiz-Clavijo, O. Caballero-Calero, M. Martín-Gonzalez, *Nanoscale* **2021**, *13*, 2227.
- [7] T. Whitney, P. Searson, J. Jiang, C. Chien, *Science* **1993**, *261*, 1316.
- [8] M. E. Toimil-Molares, *Beilstein J. Nanotechnol.* **2012**, *3*, 860.
- [9] K. Nielsch, F. Müller, A. P. Li, U. Gösele, *Adv. Mater.* **2000**, *12*, 582.
- [10] M. Rauber, I. Alber, S. Müller, R. Neumann, O. Picht, C. Roth, A. Schökel, M. E. Toimil-Molares, W. Ensinger, *Nano Lett.* **2011**, *11*, 2304.
- [11] a) E. Araujo, A. Encinas, Y. Velázquez-Galván, J. M. Martínez-Huerta, G. Hamoir, E. Ferain, L. Piraux, *Nanoscale* **2015**, *7*, 1485; b) T. da Câmara Santa Clara Gomes, J. De La Torre Medina, Y. G. Velázquez-Galván, J. M. Martínez-Huerta, A. Encinas, L. Piraux, *J. Appl. Phys.* **2016**, *120*, 043904; c) T. d. C. S. C. Gomes, J. D. L. T. Medina, Y. G. Velázquez-Galván, J. M. Martínez-Huerta, A. Encinas, L. Piraux, *IEEE Trans. Magn.* **2017**, *53*, 1; d) F. Abreu Araujo, T. da Câmara Santa Clara Gomes, L. Piraux, *Adv. Electron. Mater.* **2019**, *5*, 1800819; e) T. d. C. S. C. Gomes, F. A. Araujo, L. Piraux, *Sci. Adv.* **2019**, *5*, eaav2782; f) E. C. Burks, D. A. Gilbert, P. D. Murray, C. Flores, T. E. Felter, S. Charnvanichborikarn, S. O. Kucheyev, J. D. Colvin, G. Yin, K. Liu, *Nano Lett.* **2020**, *21*, 716.
- [12] A. Ruiz-Clavijo, S. Ruiz-Gomez, O. Caballero-Calero, L. Perez, M. Martín-Gonzalez, *Phys. Status Solidi RRL* **2019**, *13*, 1900263.
- [13] a) S. S. Parkin, M. Hayashi, L. Thomas, *Science* **2008**, *320*, 190; b) S. Parkin, S.-H. Yang, *Nat. Nanotechnol.* **2015**, *10*, 195.

- [14] A. May, M. Hunt, A. Van Den Berg, A. Hejazi, S. Ladak, *Commun. Phys.* **2019**, *2*, 13.
- [15] A. Diaz-Alvarez, R. Higuchi, P. Sanz-Leon, I. Marcus, Y. Shingaya, A. Z. Stieg, J. K. Gimzewski, Z. Kuncic, T. Nakayama, *Sci. Rep.* **2019**, *9*, 1.
- [16] a) A. Barman, G. Gubbiotti, S. Ladak, A. O. Adeyeye, M. Krawczyk, J. Gräfe, C. Adelman, S. Cotozana, A. Naeemi, V. I. Vasyuchka, *J. Phys.: Condens. Matter* **2021**, *33*, 413001; b) G. Gubbiotti, *Three-dimensional magnonics: layered, micro-and nanostructures*, CRC Press, Boca Raton, FL, USA **2019**.
- [17] R. Streubel, P. Fischer, F. Kronast, V. P. Kravchuk, D. D. Sheka, Y. Gaididei, O. G. Schmidt, D. Makarov, *J. Phys. D: Appl. Phys.* **2016**, *49*, 363001.
- [18] a) M. Charilaou, H.-B. Braun, J. F. Löffler, *Phys. Rev. Lett.* **2018**, *121*, 097202; b) J. A. Fernandez-Roldan, R. P. Del Real, C. Bran, M. Vazquez, O. Chubykalo-Fesenko, *Nanoscale* **2018**, *10*, 5923.
- [19] a) R. Hertel, presented at Spin **2013**; b) R. Hertel, *J. Phys.: Condens. Matter* **2016**, *28*, 483002; c) A. Wartelle, B. Trapp, M. Staño, C. Thirion, S. Bochmann, J. Bachmann, M. Foerster, L. Aballe, T. Menteş, A. Locatelli, *Phys. Rev. B* **2019**, *99*, 024433.
- [20] J. Escrig, R. Lavin, J. Palma, J. Denardin, D. Altbir, A. Cortes, H. Gomez, *Nanotechnology* **2008**, *19*, 075713.
- [21] A. Vansteenkiste, J. Leliaert, M. Dvornik, M. Helsen, F. Garcia-Sanchez, B. Van Waeyenberge, *AIP Adv.* **2014**, *4*, 107133.
- [22] I. Mayergoyz, *IEEE Trans. Magn.* **1986**, *22*, 603.
- [23] a) T. Peixoto, D. Cornejo, *J. Magn. Magn. Mater.* **2008**, *320*, e279; b) M. Ciureanu, F. Béron, P. Ciureanu, R. Cochrane, D. Ménard, A. Sklyuyev, A. Yelon, *J. Nanosci. Nanotechnol.* **2008**, *8*, 5725; c) R. Lavin, J. Denardin, J. Escrig, D. Altbir, A. Cortes, H. Gomez, *IEEE Trans. Magn.* **2008**, *44*, 2808; d) F. Béron, L.-P. Carignan, D. Ménard, A. Yelon, *Electrodeposited Nanowires and their Applications Vienna: IN-TECH* **2010**, 167; e) X. Kou, X. Fan, R. K. Dumas, Q. Lu, Y. Zhang, H. Zhu, X. Zhang, K. Liu, J. Q. Xiao, *Adv. Mater.* **2011**, *23*, 1393; f) E. M. Palmero, F. Béron, C. Bran, R. P. Del Real, M. Vázquez, *Nanotechnology* **2016**, *27*, 435705; g) P. Sergelius, J. G. Fernandez, S. Martens, M. Zocher, T. Böhnert, V. V. Martinez, V. M. De La Prida, D. Görlitz, K. Nielsch, *J. Phys. D: Appl. Phys.* **2016**, *49*, 145005; h) M. P. Proenca, C. T. Sousa, J. Ventura, J. Garcia, M. Vazquez, J. P. Araujo, *J. Alloys Compd.* **2017**, *699*, 421.
- [24] a) C.-I. Dobrotă, A. Stancu, *J. Appl. Phys.* **2013**, *113*, 043928; b) C.-I. Dobrotă, A. Stancu, *Phys. B* **2015**, *457*, 280; c) A. Pierrot, F. Béron, T. Blon, *J. Appl. Phys.* **2020**, *128*, 093903; d) D. A. Gilbert, G. T. Zimanyi, R. K. Dumas, M. Winklhofer, A. Gomez, N. Eibagi, J. Vicent, K. Liu, *Sci. Rep.* **2014**, *4*, 1; e) S. Ruta, O. Hovorka, P.-W. Huang, K. Wang, G. Ju, R. Chantrell, *Sci. Rep.* **2017**, *7*, 1; f) M. Rivas, P. Gorria, C. Muñoz-Gómez, J. C. Martínez-García, *IEEE Trans. Magn.* **2017**, *53*, 1; g) G. Muscas, R. Brucas, P. E. Jönsson, *Phys. Rev. B* **2018**, *97*, 174409.
- [25] C. R. Pike, A. P. Roberts, K. L. Verosub, *J. Appl. Phys.* **1999**, *85*, 6660.
- [26] G. Muscas, M. Menniti, R. Brucas, P. Jönsson, *J. Magn. Magn. Mater.* **2020**, *502*, 166559.
- [27] A. Elmekawy, E. Iashina, I. Dubitskiy, S. Sotnichuk, I. Bozhev, K. S. Napolskii, D. Menzel, A. Mistonov, *Mater. Today Commun.* **2020**, *25*, 101609.
- [28] J. García Fernández, V. Vega Martínez, A. Thomas, V. M. De la Prida Pidal, K. Nielsch, *Nanomaterials* **2018**, *8*, 548.
- [29] Y. P. Ivanov, M. Vázquez, O. Chubykalo-Fesenko, *J. Phys. D: Appl. Phys.* **2013**, *46*, 485001.
- [30] M. Proenca, J. Ventura, C. Sousa, M. Vazquez, J. Araujo, *J. Phys.: Condens. Matter* **2014**, *26*, 116004.
- [31] a) F. Béron, L.-P. Carignan, D. Ménard, A. Yelon, *IEEE Trans. Magn.* **2008**, *44*, 2745; b) A. Rotaru, J.-H. Lim, D. Lenormand, A. Diaconu, J. B. Wiley, P. Postolache, A. Stancu, L. Spinu, *Phys. Rev. B* **2011**, *84*, 134431; c) E. M. Palmero, M. Méndez, S. González, C. Bran, V. Vega, M. Vázquez, V. M. Prida, *Nano Res.* **2019**, *12*, 1547.
- [32] F. Béron, M. Knobel, K. R. Pirota, *J. Phys. D: Appl. Phys.* **2012**, *45*, 505002.
- [33] J. Gräfe, M. Weigand, C. Stahl, N. Träger, M. Kopp, G. Schütz, E. J. Goering, F. Haering, P. Ziemann, U. Wiedwald, *Phys. Rev. B* **2016**, *93*, 014406.
- [34] L. Sun, C. Zhou, J. Liang, T. Xing, N. Lei, P. Murray, K. Liu, C. Won, Y. Wu, *Phys. Rev. B* **2017**, *96*, 144409.
- [35] C. Li, W. Yin, H. Jiang, Y. Zhang, *Comput. Optim. Appl.* **2013**, *56*, 507.
- [36] M. López-Haro, M. Tinoco, S. Fernández-García, X. Chen, A. B. Hungria, M. Á. Cauqui, J. J. Calvino, *Part. Part. Syst. Charact.* **2018**, *35*, 1700343.
- [37] M. Dimian, P. Andrei, presented at Journal of Physics: Conference Series **2015**.
- [38] J. A. Fernández-Roldán, Y. P. Ivanov, O. Chubykalo-Fesenko, in *Magnetic Nano-and Microwires*, Elsevier, Amsterdam **2020**, p. 403.